Geophysical Research Letters

RESEARCH LETTER
10.1029/2025GL116440

The Role of Stress Distribution in Seismic Cycle Complexity of a Long Laboratory Fault

F. Paglialunga[1], F. Passelègue[1], J. P. Ampuero[1], S. Latour[2], and M. Violay[3]

[1]Université Côte d'Azur, CNRS, Observatoire de la Côte d'Azur, IRD, Géoazur, Sophia Antipolis, Nice, France, [2]Université de Toulouse, CNRS, Observatoire Midi-Pyrénées, IRAP, Toulouse, France, [3]École Polytechnique Fédérale de Lausanne, Lausanne, Switzerland

Abstract A fundamental understanding of the factors controlling the complexity of seismic cycles is crucial to advance the study of earthquake hazard and predictability. Stress distribution and fault system size play a significant role in shaping complex patterns of seismic behavior. This study examines how heterogeneous loading conditions influence the seismic cycles of a long laboratory fault. They are reproduced on analog material in a biaxial apparatus while continuously monitoring the strain field near the fault. By examining the effects of stress variability on fault behavior, we identify a spectrum of rupture outcomes, from periodic, system-size failures to complex seismic sequences comprising several partial ruptures. Additionally, the resulting heterogeneous stress distribution significantly influences single events' rupture dynamics, eventually leading to abrupt rupture slowdown and subsequent delayed re-nucleation. These results provide a framework for understanding the evolution of stress heterogeneity along natural faults and its implications for rupture dynamics and earthquake predictability.

Plain Language Summary Earthquakes present a serious threat to our society, causing loss of life and economic damage. Understanding what controls their occurrence (i.e., the seismic cycle) is essential for effective hazard assessment. However, natural faults are difficult to study directly, and their geometry and stress conditions are poorly constrained. To address this, we develop an experimental study that simulates the main rupture behavior on a long artificial fault (i.e., analog material sample), simplifying the system for a better understanding. Using a high-frequency acquisition system, we could monitor the stress evolution along the fault and emphasize the importance of its distribution. In particular, heterogeneous stress along the fault was found (a) to cause complex seismic sequences, with multiple partial events occurring between major ruptures, and (b) to strongly affect the dynamics of individual ruptures.

Key Points:

- Loading conditions strongly influence stress distribution and rupture nucleation location
- Heterogeneous fault stress promotes the transition from system-size to complex seismic cycles
- Heterogeneous stress influences rupture dynamics, leading to abrupt decelerations and delayed secondary rupture

Supporting Information:

Supporting Information may be found in the online version of this article.

Correspondence to:

F. Paglialunga,
federica.paglialunga@geoazur.unice.fr

Citation:

Paglialunga, F., Passelègue, F., Ampuero, J. P., Latour, S., & Violay, M. (2025). The role of stress distribution in seismic cycle complexity of a long laboratory fault. *Geophysical Research Letters*, *52*, e2025GL116440. https://doi.org/10.1029/2025GL116440

Received 11 APR 2025
Accepted 18 AUG 2025

Author Contributions:

Conceptualization: F. Paglialunga, F. Passelègue, M. Violay
Data curation: F. Paglialunga
Formal analysis: F. Paglialunga, F. Passelègue
Funding acquisition: F. Passelègue, M. Violay
Investigation: F. Paglialunga, F. Passelègue, J. P. Ampuero, S. Latour, M. Violay
Resources: F. Passelègue, M. Violay
Software: J. P. Ampuero, S. Latour
Supervision: F. Passelègue, J. P. Ampuero, M. Violay
Validation: F. Paglialunga, F. Passelègue, J. P. Ampuero, M. Violay
Visualization: F. Paglialunga
Writing – original draft: F. Paglialunga

1. Introduction

Understanding the relationship between along-fault stress distribution and fault behavior is a fundamental challenge in earthquake science, with significant implications for seismic hazard assessment. Natural fault systems are controlled by many interacting factors that govern rupture nucleation, propagation, and arrest. Among these factors, initial along-fault stress distribution is a key driver of rupture dynamics, influencing seismic events' size, recurrence interval, and spatial characteristics. Das and Aki (1977) demonstrated that a stress barrier can affect the rupture dynamics and the general shape of slip profiles. Caniven et al. (2017) showed through a scaled seismotectonic model how spatial variations of fault normal stress "control the ability of the fault to generate irregular or regular seismic cycles and produce clustering sequences." Such complex seismic cycles are also known as supercycles (Salditch et al., 2020).

Together with stress heterogeneity, another key aspect contributing to the complexity of the seismic cycle is the system size. In particular, the ratio between the fault length L and the cohesive zone size x_c is pivotal. For large $\frac{L}{x_c}$, Lapusta and Rice (2003) highlighted the emergence of partial ruptures between complete events that break the whole fault, sharing similar nucleation characteristics. Cattania (2019) demonstrated that a larger $\frac{L}{L_c}$ ratio, with L_c the rupture nucleation size, leads to complex earthquake sequences, even on planar faults with homogeneous frictional properties, when the system is driven by heterogeneous loading that spontaneously emerges due to imposed fault creep outside the seismogenic zone. Moreover, the interplay between system size and frictional fault properties also governs the complexity of seismic sequences (Barbot, 2019). The occurrence of partial events implies the arrest of a propagating rupture. This condition is favored in long fault systems (Ke et al., 2020) and

Writing – review & editing:
F. Paglialunga, F. Passelègue,
J. P. Ampuero, S. Latour, M. Violay

likely enhanced by heterogeneous stress distributions (Bayart et al., 2018; Buijze et al., 2020; Cebry et al., 2023; Radiguet et al., 2013, 2015; Tinti et al., 2005).

However, studying the role of stress heterogeneity in seismic behavior is challenging because earthquakes typically occur at significant depths. Except for rare cases (Bakun et al., 2005), instrumenting faults and gaining insights into their loading and geometrical conditions remains challenging. One promising solution is replicating earthquakes on artificial faults under controlled laboratory settings equipped with advanced acquisition systems. While simplifying natural fault systems, especially their rheology and geometry, this approach allows investigation of many key aspects of seismic activity, leading to valuable insights into earthquake physics and mechanics (Brace & Byerlee, 1966; Bayart et al., 2018; Chen et al., 2021; Cebry et al., 2023; Corbi et al., 2024; Fryer et al., 2024; Gvirtzman & Fineberg, 2021; Lu et al., 2007; Rosakis et al., 1999; G. Mclaskey, 2019; G. C. Mclaskey & Kilgore, 2013; Mastella et al., 2022; Passelègue et al., 2013; Rubino et al., 2022; Rubino & Rosakis, 2020; Selvadurai, 2019; Svetlizky & Fineberg, 2014; Tal et al., 2022; Xia et al., 2004).

Large-scale friction experiments on rocks have so far unveiled important features of laboratory earthquakes (Dieterich, 1978, 1981; Ke et al., 2018, 2020; Okubo & Dieterich, 1981, 1984; Yamashita et al., 2018, 2021). However, despite their significant size, their ratio L/L_c remains small compared to what is expected in nature. Using analog materials, which have smaller elastic moduli and critical slip distances than rocks, allows for an increase in the $\frac{L}{L_c}$ ratio by an order of magnitude compared to rock fault interfaces (Bayart et al., 2016, 2018; Buijze et al., 2020, 2021; Cebry et al., 2022; Gounon et al., 2022; Guérin-Marthe et al., 2019; Latour et al., 2013; Rosakis et al., 1999; Rubino et al., 2022; Svetlizky et al., 2017; Svetlizky & Fineberg, 2014). In this study, we present new experimental results highlighting the influence of heterogeneous stress distributions on the seismic behavior of a laboratory fault with an unprecedented ratio $\frac{L}{L_c} \sim 100$. Our results demonstrate that a heterogeneous loading can (a) affect the nucleation location of instabilities, (b) increase the number of partial events occurring between complete ruptures, and (c) induce complex dynamic rupture propagation processes.

2. Experimental Setup and Methods

A large biaxial apparatus was built in the Laboratory of Experimental Rock Mechanics at the Swiss Federal Institute of Technology of Lausanne (EPFL). This apparatus allows for a ratio of $\frac{L}{L_c} \sim 100$, considering $L_c \simeq 2$–3 cm for a range of normal stress of ∼2–3 MPa (Paglialunga et al., 2023). Two samples are pressed together and successively sheared in a direct single-shear configuration to produce frictional ruptures. This setup hosts analog material samples (2.5 × 0.5 × 0.03 m) that can slip along a 2.5 × 0.03 m artificial interface (Figure 1a, Figure S1 in Supporting Information S1). The samples are made of Poly (methyl methacrylate) (i.e., PMMA), characterized by S-wave velocity C_s = 1,350 m/s, Rayleigh wave velocity C_R = 1,242 m/s, and P-wave velocity C_p = 2,700 m/s. The normal load is applied via 20 hydraulic pistons across four distribution plates, for a final normal stress distribution along the fault between 1 and 4 MPa (Figure 1b). Shear load is applied via five pistons, loading the lower sample's lateral side at an elastic loading rate of 0.44 MPa/s (Figure 1a).

The distribution of the applied stress along the fault was controlled thanks to five different stopper configurations (Figure 1a). This boundary condition enables modification of the external loading, thereby influencing the stress distribution along the fault (Iwashita et al., 2023) (Figure S2 in Supporting Information S1). The first configuration used a 50 cm stopper spanning the full sample height, referred to as the "large stopper" (green). The second and third used a 20 cm stopper placed at 28 cm ("top-medium stopper", yellow) and 9 cm ("bottom-medium stopper", blue) from the fault. The fourth and fifth used an 8.5 cm stopper at 38 cm ("top-small stopper", purple) and 9 cm ("bottom-small stopper", orange) from the fault. Each configuration defined a different initial normal and shear stress distribution (Figure 1b, Table S1 in Supporting Information S1).

Strain evolution along the fault was monitored using strain gauges measuring at a frequency of 40 kHz (National Instrument system). Rosettes (i.e., arrangement of three strain gauges oriented at 45°, 90°, and 135°to the fault plane) were placed ∼3 mm away from the fault at nine locations, with eight usable simultaneously (Figure 1a). Stress tensors were derived assuming plane stress conditions (see Text S1, S2 in Supporting Information S1 for details).

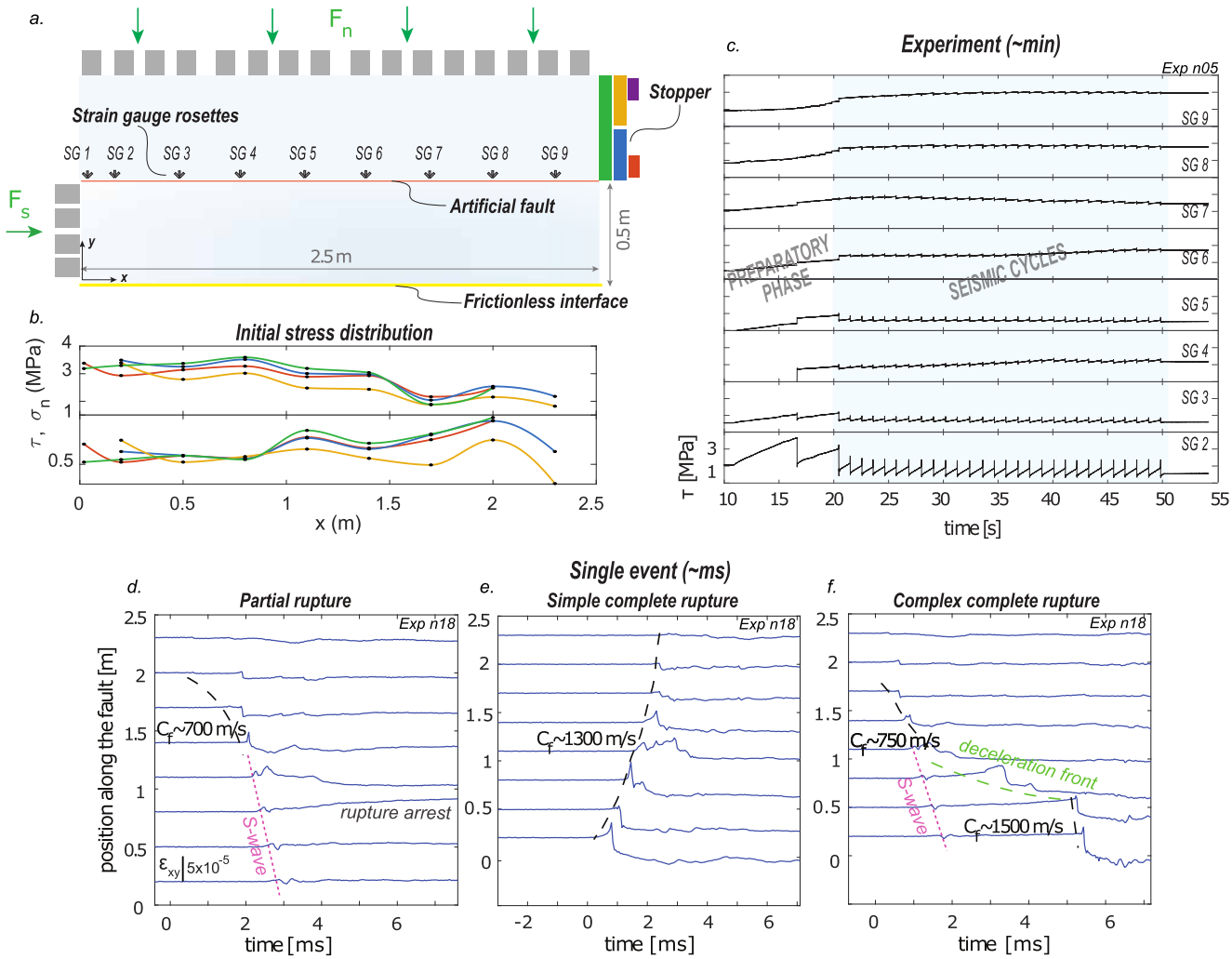

Figure 1. (a) Sketch of the large biaxial apparatus. Distinct colors indicate different stopper configurations. (b) Normal and shear stress distribution obtained under each stopper configuration and spatially interpolated (colors refer to stopper in (a)). Black markers indicate strain gauge locations along the fault. (c) Temporal evolution of shear stress throughout one representative experiment (n05), at eight measuring locations (SG2-SG9). Strain measurement during (d) partial, (e) complete, and (f) complex events observed in experiment n18. Solid blue curves indicate the shear strain temporal evolution. Black dashed lines indicate the rupture propagation front, purple dotted curves the S-wave front, and green dashed curves the deceleration front.

3. Results

3.1. Laboratory Earthquakes

Across all experiments conducted, the fault behavior exhibited rich and yet qualitatively consistent sequences of rupture events for each given initial configuration. The fault accommodated the shear stress increase through a preparatory phase involving several partial ruptures (Kammer et al., 2015; Rubinstein et al., 2004), followed by a sequence of recurrent seismic cycles, including ruptures that propagated along the entire fault length (Figure 1b).

Three principal types of events were identified: partial (Figure 1d), complete (Figure 1e), and complex ruptures (Figure 1f). Partial ruptures predominantly nucleated around $x = 2.3$ m, where x is the position along the fault relative to the forcing edge (left) of the sample, and accelerated into dynamic propagation (dashed black lines). They reached a speed of ~700 m/s ($\simeq 0.52\ C_s$), then decelerated and arrested before reaching the sample's edge. The arrest caused localized strain accumulation in the unruptured region (Figure 1d). Simple complete ruptures nucleated at $x = 0$ m and dynamically propagated across the entire fault at an average rupture velocity of ~1,250 m/s ($\sim C_r$, the Rayleigh wave speed) (Figure 1e). However, most complete ruptures exhibited complex dynamics (Figure 1f). These events generally nucleated near $x = 2.3$ m and promptly accelerated to a speed of

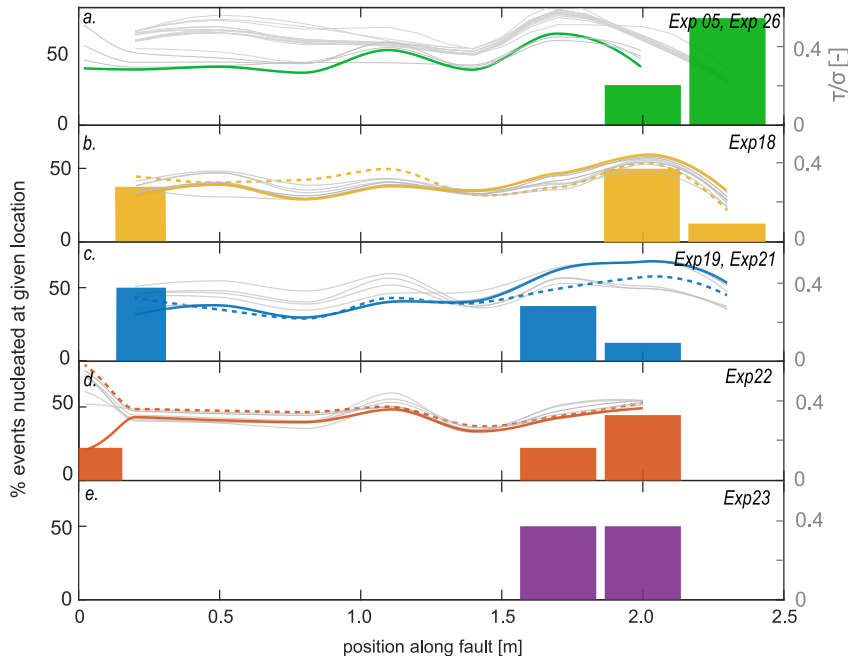

Figure 2. Distribution of event nucleation locations along the fault for different initial boundary conditions. The color legend refers to Figure 1. Labels on top right indicate the experiments used to recreate the plot (a–e). In gray, the distribution of $\frac{\tau}{\sigma_{yy}}$ before each studied rupture. In colored solid lines and dashed lines, the distribution before selected ruptures nucleating at $x = 2.0$ m and $x = 0$ m respectively. Note that the initial stress distribution is not available for experiment n23 (top-small stopper).

~750 m/s. The rupture front was halted at $x = 1.1$ m, resulting in a slow but continuous strain accumulation over 0.5 m. It then re-nucleated and propagated through the remaining fault length at supershear velocity (~1,500 m/s).

3.2. Influence of Initial Stress Distribution on Rupture Nucleation

The nucleation location of system-size events (i.e., simple and complex) was determined as the location of the strain gauge that experienced a first strain perturbation. We focused on system-size events, as partial ones consistently nucleated on the same portion of the fault (~$x = 2.0$ m), in line with previous, extensively studied observations (Kammer et al., 2015; Rubinstein et al., 2011). The distributions of $\frac{\tau}{\sigma_{yy}}$ before each rupture event, interpolated between the measurement locations, are shown by the gray solid lines in Figure 2.

Our results confirm that the external boundary conditions control the rupture nucleation locations. When the large or the top-small stopper was employed, all ruptures consistently nucleated around ~$x = 2.0$ m (Figures 2a and 2e). Notably, with the top-small stopper, the average nucleation location shifted slightly toward the central part of the fault (Figure 2e). In contrast, other stopper configurations resulted in nucleation occurring on both fault sides (i.e., $x = 0$ m, $x = 2$ m, Figures 2b–2d). For the top-medium stopper, 62% of the events nucleated around $x = 2.0$ m, while 38% occurred around $x = 0$ m. The bottom-medium stopper exhibited the most balanced distribution, with nearly 50% of events nucleating on each side of the fault ($x = 0$ m and $x = 2.0$ m). Lastly, the bottom-small stopper predominantly induced nucleation at around $x = 2.0$ m, with only 22% of simple ruptures originating at $x = 0$ m.

A representative friction profile recorded before an event nucleating at ~$x = 2.0$ m ($x = 0$ m) is shown as solid (dashed) colored lines. At first order, the nucleation occurs where $\frac{\tau}{\sigma_{yy}}$ reaches its highest value. Events nucleating at $x = 2.0$ m coincided with the highest $\frac{\tau}{\sigma_{yy}}$ values, measured as 0.41, 0.44, 0.52, and 0.38 for the large, top-medium, bottom-medium, and top-small stopper, respectively (solid colored lines, Figures 2a–2d). This trend was confirmed for events nucleating at $x = 0$ m in experiments where strain gauge data were available on that portion of the fault. For instance, with the top-small stopper configuration, ruptures nucleated at a local $\frac{\tau}{\sigma_{yy}}$ value of 0.59 (Figure 2d, orange dashed curve).

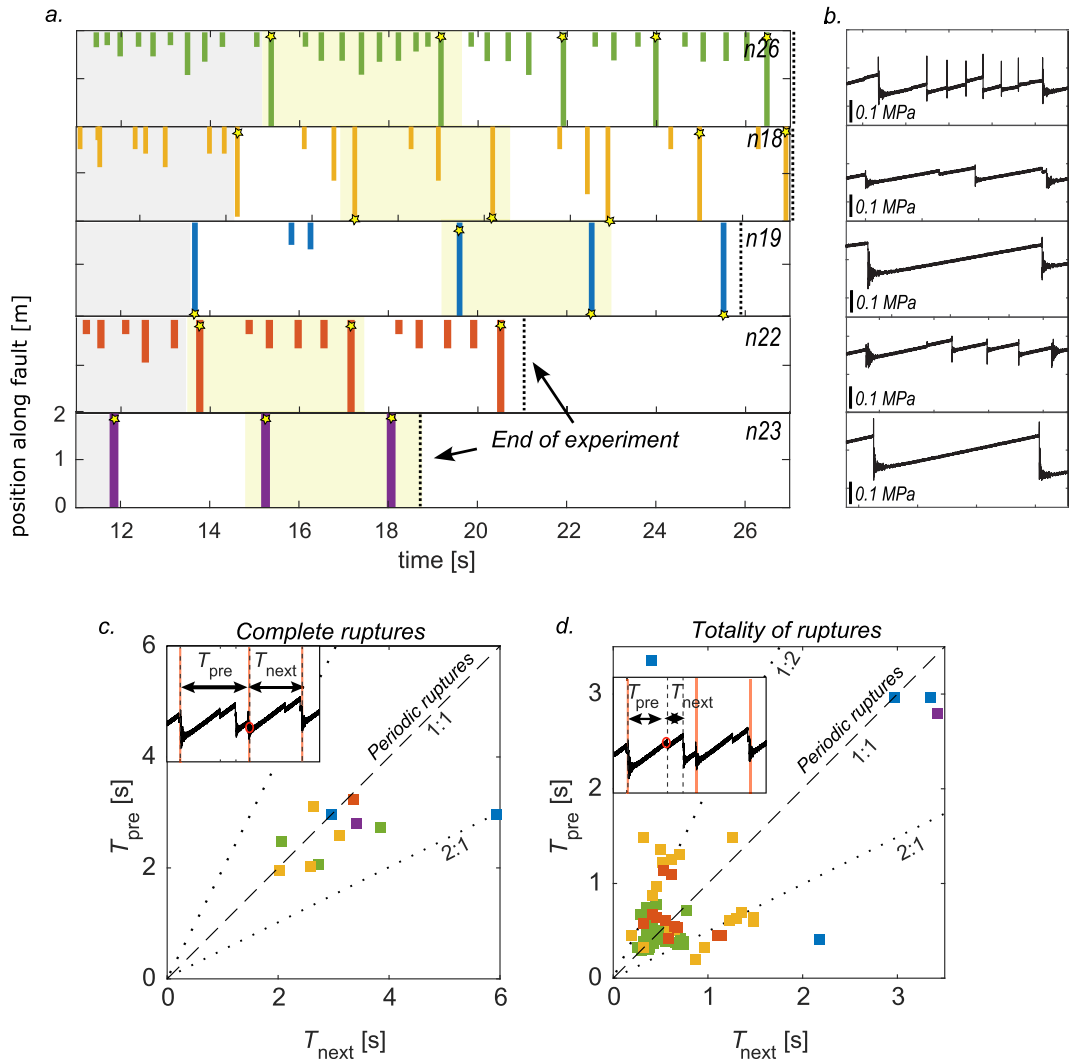

Figure 3. (a) Occurrence time and rupture length for all the events in selected experiments (from top to bottom: n26, n18, n19, n22, n23). Due to sensor placement, complete ruptures spanning the full 2.5 m fault appear as 2 m long. Stars indicate the nucleation location of complete ruptures. The dotted black line indicates the end of the experiments. The gray area indicates the preparatory phase before the first complete event. The yellow area indicates the selected sequences shown in (b). (b) Shear stress evolution for a representative seismic sequence, measured by strain gauge SG7 ($x = 1.7$ m). Inter-event times are computedfor complete ruptures (c) only and for all events (d), partial and complete. Color legend follows the one indicated in Figure 1. Note that for this recurrence time analysis, only the initial portion of each experiment is considered to avoid bias from pauses in shear stress loading that occur later during the experiment. As a result, the percentage of nucleation locations reported here differs from those in Figure 2, since a smaller subset of ruptures is shown.

3.3. From System-Size Events to Complex Seismic Sequences

The observed seismic sequences exhibited a wide range of behaviors, from systematic complete ruptures to complex seismicity patterns. For each event, the rupture length was determined based on the fault segment that exhibited a sudden shear stress drop, a hallmark of rupture propagation (Figure 3a). The resolution of this measurement relies on the spatial arrangement of the strain gauges along the fault.

External loading conditions exerted by the different stopper configurations controlled the complexity of the seismic sequences. Experiments with large stopper revealed the most diverse rupture size distribution, with an average of six partial ruptures occurring between two complete ruptures (Figure 3a). In contrast, experiments with top-medium stopper yielded an average of two partial ruptures between consecutive complete ruptures. Experiments conducted with bottom-medium stopper were predominantly characterized by system-size events,

consisting of complete ruptures occurring at regular intervals. Bottom-small stopper experiments exhibited a more complex distribution, with an average of four partial ruptures occurring between two complete ruptures. Finally, experiments involving top-small stopper were dominated by quasi-periodic complete ruptures.

The patterns of inter-event times provide further insight into how the stress distribution influences the complexity of the seismic cycle. We define two distinct time intervals: $T_{\mathbf{pre}}$ is the time elapsed between a given event and the one preceding it, and $T_{\mathbf{next}}$ is the time between an event and the subsequent one (Gualandi et al., 2023; Mei et al., 2021; Mele Veedu et al., 2020). For events occurring periodically $T_{\mathbf{pre}} = T_{\mathbf{next}}$, while for events not occurring periodically $T_{\mathbf{pre}} \neq T_{\mathbf{next}}$. This analysis was performed for each stopper configuration by considering (a) complete events only (Figure 3c) and (b) all events, including both partial and complete ruptures (Figure 3c). The inter-event times between complete events show almost periodic behavior (with values ranging between 2 and 6 s, Figure 3d). The only exception is an example of cycle skipping in experiment n19 (in blue in Figure 3), where the second expected complete rupture unexpectedly occurred as a slow slip event. The latter interestingly showed a faint drop of stress without the sharp and pronounced stress drop observed in fast rupture events, and was followed by a reduced loading rate for an extended portion of the fault, until the next complete rupture (Figure S2 in Supporting Information S1). Unfortunately, stress measurements are not sufficient to fully describe and constrain the nature of this event. When considering the totality of events (Figure 3c), the inter-event times ranged between 0.1 and 1.5 s for the complex sequences (experiments n26, n18, and n22) and between 2.1 and 3.5 s for the system-size sequences (experiments n19, n23). Many of them, mostly partial ruptures, occurred periodically (Figure 3d). This happened for 70%, 21%, 50%, 42%, and 100% of the total number of events respectively for experiments n26, n18, n19, n22, n23.

Interestingly, the inter-event times of the events that deviate from periodicity tend to cluster along different slopes, suggesting that the fault behavior tends toward a periodic pattern. This is evident for experiment n18, where the second, third, and fourth sequences follow a similar pattern: a longer inter-event time after a complete rupture, followed by two shorter inter-event times after partial ruptures. A similar trend is observed in experiment n22. In these events, the inter-event time seems governed by the static friction drop experienced by the preceding rupture at the nucleation site. Larger friction drops lead to longer inter-event times (Figure S3 in Supporting Information S1). Notably, the large static friction drops associated with complete ruptures are influenced by post-seismic activity, such as secondary ruptures and wave reflections, which are absent or minimal in the case of partial ruptures. These processes further weaken the fault, resulting in a larger static stress drop. At the same time, such post-seismic activity delays the fault's re-locking and subsequent re-loading. The magnitude of this effect depends on the stress distribution, leading to a range of $\frac{T_{\mathbf{next}}}{T_{\mathbf{pre}}}$ values between 1 and 4.

4. Discussion

4.1. Emergence of Complexity in Seismic Cycles

The initial stress distribution controlled the nucleation location of the rupture events, which occurred at different positions along the fault. In particular, the nucleation locations are influenced by the local stress ratio $\frac{\tau}{\sigma_{yy}}$, and mostly occurred at the places where it was maximal. This observation is consistent with previous studies that highlight that rupture nucleation tends to occur where $\frac{\tau}{\sigma_{yy}}$ is maximal (Ben-David & Fineberg, 2011; Buijze et al., 2020). However, we also observed that the values of $\frac{\tau}{\sigma_{yy}}$ at nucleation were not fixed but ranged between 0.35 and 0.6 (values sensitive to the spatial resolution of our measurements). So, while $\frac{\tau}{\sigma_{yy}}$ plays a key role in controlling the onset of rupture, it is not a sufficient nucleation criterion, as recently pointed out (Gvirtzman & Fineberg, 2023). Other nucleation models show that various quantities can, in fact, significantly contribute; e.g., potential and fracture energies influence nucleation through quasi-static crack growth in the large-scale yield regime (e.g., Rubin & Ampuero, 2005).

The heterogeneous stress distribution not only influenced rupture nucleation but also shaped the overall seismic cycle, leading to the emergence of finite rupture events between complete ruptures (Figure 3), as anticipated by large-scale experiments (Caniven et al., 2017). The seismicity statistics surrounding a major event are generally explained by the frictional properties of faults (Dublanchet et al., 2013; Kaneko et al., 2010; Wang et al., 2024) or geometrical characteristics (Dal Zilio et al., 2019), but even a single homogeneous fault can exhibit complex behavior if sufficiently long (Cattania, 2019). Our experiments integrate these conditions. The seismic cycles

occurred on a single fault (L = 2.5 m) approximately 100 times larger than the expected nucleation length (L_c = 2.5 cm (Latour et al., 2013; Paglialunga et al., 2023)). According to Cattania (2019), such a high $\frac{L}{L_c}$ ratio is sufficient to induce the occurrence of sub-system-size events in the presence of a heterogeneous loading distribution.

More precisely, the emergence of partial ruptures can be explained through an energetic perspective. In Linear Elastic Fracture Mechanics, rupture propagation occurs when the energy release rate (G) at the rupture tip exceeds the fracture energy (G_c), which resists rupture propagation (Freund, 1979). If the available energy is insufficient, the rupture will arrest. This can occur due to either a reduction in G or an increase in G_c. In our experimental seismic sequences, multiple ruptures sequentially arrested when the energy release rate fell below the fracture energy ($G < G_c$) (Figure S5 in Supporting Information S1). This arrest increased shear stress in the unruptured section of the fault, raising the energy available for subsequent ruptures (Figures S5d and S5e in Supporting Information S1). Eventually, this process led to full rupture propagation once G exceeded G_c along the entire fault. This analysis aligns with previous rupture length predictions (Bayart et al., 2016; Kammer et al., 2015; Ke et al., 2018) (Text S3 in Supporting Information S1).

In some sequences, the temporal evolution of stress reveals that, as the shear stress approaches its critical distribution (i.e., as represented by the bright green curve in Figure S5c in Supporting Information S1), the local stress increase generated by the arrest of the preceding partial rupture gradually diminishes. This trend culminates in an almost imperceptible stress rise, ultimately leading to a complete rupture. Although this phenomenon does not occur in all the sequences analyzed, it underscores how, under certain stress conditions, even a small change in shear stress can significantly influence the final rupture size (Figure S4 in Supporting Information S1).

Our experiments also provide valuable insight into interevent times. For complex sequences (experiments n26, n18, n22), when considering all events, their occurrence seems aperiodic, with inter-event times ranging from 0.2 to 1.5 s (Figure 3d). However, a closer examination reveals a tendency of the fault toward periodic patterns. In particular, most partial ruptures occurred quasi-periodically with short interevent times (0.2–0.5 s), whereas complete ruptures were often followed by longer intervals (0.5–1.5 s). This behavior is governed by the heterogeneous stress distribution along the fault and controlled by the friction drop experienced by the preceding rupture (Figure S3 in Supporting Information S1). This is coherent with the slip-predictable model, for which the interevent time is controlled by the coseismic slip of the preceding earthquake (Shimazaki & Nakata, 1980). Such phenomenon has also been employed as an indirect method for mapping seismic asperities in space (Wyss et al., 2000). In contrast, considering complete ruptures only, they exhibit overall quasi-periodic recurrence, with inter-event times of 2–6 s (Figure 3c). Their coefficient of variation, defined as $\mathrm{CV}(\%) = \left(\frac{\mathrm{SD}}{\bar{x}}\right) \times 100$, where SD is the standard deviation and $\bar{x}$ the mean value, was calculated. The resulting CV were 23%, 18.6%, 39.9%, 6%, and 23.5% respectively for experiments n26, n18, n19, n22, n23. Note that these estimates rely on the available data sample, specifically, the complete ruptures shown in Figure 3a were used in the calculation (with 3, 6, 4, 3, and 3 ruptures, respectively). The cycles involving only system-size events (associated with lower stress heterogeneity) tend to have slightly longer average recurrence times compared to cycles with multiple ruptures (associated with higher stress heterogeneity). This finding is consistent with the simulations of Cattania and Segall (2021), which show that rough faults exhibit longer recurrence times than smooth ones, suggesting that fault properties and stress heterogeneity may exert similar effects on periodicity. Ultimately, our observations highlight that the on-fault stress distribution dictates a first-order recurrence time, resulting in quasi-periodic complete ruptures (Figure 3c). This recurrence time can, however, be altered (expanded or shortened) by the emergence of partial ruptures or slow slip events influenced by local stress heterogeneity.

4.2. Influence of Stress Heterogeneity on Rupture Dynamics

Most complete ruptures observed in these experiments exhibit complex rupture processes (Figure 1f). They generally nucleated near the leading edge (x = 2.0 m) and accelerated to a rupture speed of approximately 0.5 C_s. After propagating over 0.5 m, they decelerated to transient velocities ranging from 650 m/s to 56 m/s (i.e., 0.45 to 0.05 C_s), depending on the event, over ∼0.7 m. The transient propagation of the rupture within this region was accompanied by a stress build-up over a period defined as t_{delay} (Figure 4). Following this delay, the rupture re-accelerated, propagating at supershear velocities.

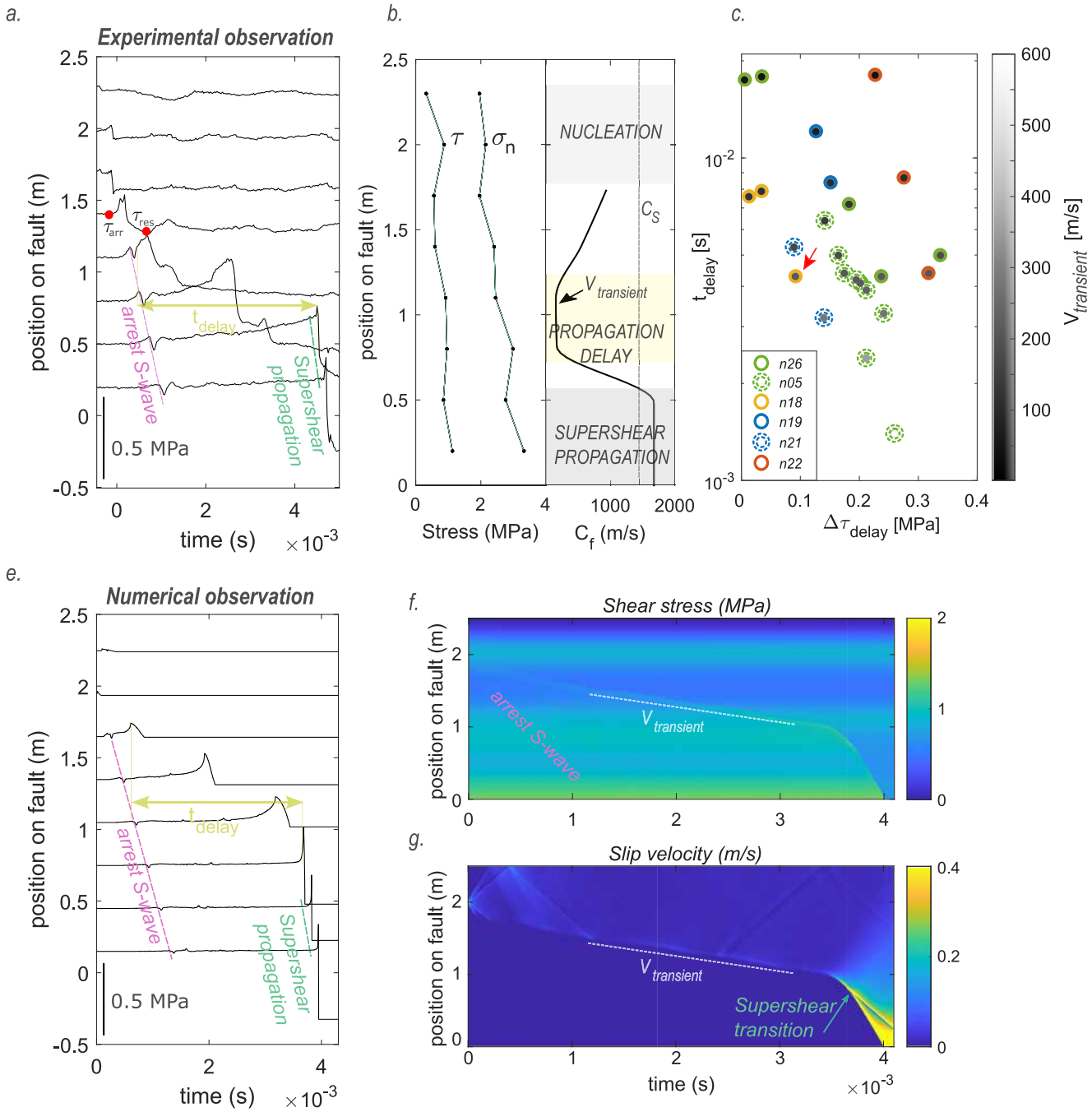

Figure 4. (a) Representative complex event from experiment n18. Temporal shear stress evolution at all gauge locations. The time delay is indicated in yellow. Red markers indicated τ_{arr} and τ_{res}. (b) Shear and normal stress distribution before the event (on the left) and rupture speed (on the right). (c) t_{delay} and $\Delta\tau_{delay}$ for all ruptures, showing a linear trend within experiments, indicating stress controls delay and velocity. The red arrow points to the selected event in (a). (d) Numerical simulation of complex rupture. Temporal evolution of shear stress at equidistant fault locations. (e, f) Spatiotemporal evolution of shear stress and slip velocity.

The rupture delay time t_{delay} was measured as the interval between the two distinct and abrupt stress drops, markers of dynamic propagation, before and after deceleration. It varied significantly across the different complex ruptures observed, spanning more than an order of magnitude, from 1.4 to 18 ms (Figure 4). t_{delay} appeared to be controlled by the background stress level at the deceleration location. Effectively, for each loading condition, t_{delay} decreased linearly with $\Delta\tau_{delay}$, defined as $\tau_{arrest}-\tau_{res}$, with τ_{arrest} the background shear stress at the deceleration location, and τ_{res} the residual shear stress at that same location. Large values of $\Delta\tau_{delay}$ induced larger transient

velocities within the stress barrier, resulting in shorter t_{delay}. Note that $\Delta\tau_{delay}$ serves as a direct proxy for the efficiency of the barrier: a large $\Delta\tau_{delay}$ indicates an initial stress state close to the fault frictional strength. This behavior is consistent with LEFM theory, for which the propagation velocity strictly depends on the G/G_c ratio $\left(C_f = f(G/G_c)\right)$ (Freund, 1979). A low $\Delta\tau_{delay}$ will lead to a low G/G_c, resulting in a localized velocity reduction. However, the spatial resolution of our measurements does not allow us to quantify such a reduction.

To overcome this limitation and confirm the crucial role of the heterogeneous stress distribution, numerical simulations were conducted using the spectral element software SEM2DPACK (Ampuero, 2012). A representative complex event from experiment n18 was selected and reproduced numerically (partial and complete ruptures were also reproduced, Text S4, Figure S10 in Supporting Information S1). A linear slip-weakening friction law was used. The critical slip distance, the static and residual friction, and the initial stress distribution were extrapolated from experimental observations (i.e., heterogeneous distribution, Figure S9 in Supporting Information S1). The nucleation was forced through a region of overstress imposed at $x = 2.0$ m, as observed in the selected experimental event.

The numerical simulation qualitatively reproduced the experimental observations, capturing a similar complex rupture propagation process (Figures 4e–4g). Upon nucleation, the rupture propagated bilaterally. The rightward-propagating front exhibited a variable subshear velocity until it reached the fault edge. The leftward-propagating front also traveled at a subshear velocity before decelerating abruptly at $x = 1.7$ m. Such a pronounced deceleration caused radiation of stopping waves that reduced slip velocity in the wake of the rupture tip. S-waves were also radiated ahead of the rupture front (Figure 4e). The rupture propagated at a significantly reduced velocity (i.e., $V_{transient}$) for a distance of ∼0.7 m. Moreover, S-waves previously radiated by the rupture were reflected at the fault edges. Upon re-entering the barrier, these reflected waves locally enhanced slip through a step-like increase. Despite the drastically reduced propagation velocity, the rupture eventually reached a shear stress level sufficient to resume dynamic propagation, transitioning to supershear velocity (Figure 4).

The numerical simulation qualitatively replicates the experimental conditions, providing valuable insights into interpreting our observations. It underscores the significant influence of heterogeneous stress on rupture dynamics, which can markedly alter the propagation behavior without necessarily stopping the rupture. Similar complexities in rupture dynamics have been highlighted in recent work, where a rupture propagation could be either arrested or enhanced by a normal stress heterogeneity, depending on its strength (Cebry et al., 2023). In particular, this process bears similarities to the observed creep fronts in laboratory experiments on analog materials containing quartz gouge faults (Cebry et al., 2022). However, in those experiments, delayed triggering was attributed to a combination of initial overstress and the frictional properties of the gouge. These observations collectively highlight that rupture extent (i.e., whether a rupture will be partial or complete) can be highly sensitive to the underlying stress distribution.

One could argue that these complex ruptures correspond to two distinct seismic events. The time delay between the two propagation phases is one to two orders of magnitude larger than the early dynamic propagation phase. This result questions the definition of the rupture event itself, where the second propagation phase could be interpreted as an early aftershock or, if of comparable size, as a doublet earthquake (Sladen et al., 2010). A famous example is the 2007 Mw 8.0 Pisco earthquake (Perfettini et al., 2010). This earthquake ruptured two well-separated asperities with a time delay of around 60 s. The resolution of the modeling could not constrain whether the rupture jumped from the first to the second asperity or continued slowly between them (Sladen et al., 2010). A more recent example of complex rupture is the 2024 Mw 7.5 Noto earthquake (Xu et al., 2024). After nucleation, the rupture was significantly slowed down by an asperity. After a time delay of ∼10 s, a new rupture was triggered on the opposite side of the asperity, eventually breaking it, and resulting in large coseismic slip. Despite different factors that could have contributed to this behavior, as the frictional properties of the fault, the local stress distribution offers a valid interpretation. Our experimental results demonstrate that stress distribution significantly influences rupture dynamics, offering new insights into the interpretation of natural earthquakes.

5. Conclusions

Our results demonstrate that heterogeneous initial stress conditions along an extended experimental fault can shift seismic cycle behavior from system-size, quasi-periodic ruptures to cycles exhibiting greater complexity. This

complexity manifests in the occurrence time of ruptures, their nucleation location, and size. These findings support the idea that a detailed investigation of the seismicity spatial and temporal evolution along natural fault systems could help elucidate the evolution of stress distribution. Furthermore, we highlight the pivotal role of stress heterogeneity in controlling the rupture dynamics of single events. We observed complex ruptures marked by strong deceleration caused by stress heterogeneity, followed by abrupt re-acceleration. This behavior sheds light on the variability of seismic events, suggesting that, depending on the strength and distribution of heterogeneity, a rupture may either remain confined to a smaller scale or escalate into a larger event.

Data Availability Statement

The data used in this study are publicly available at Paglialunga et al. (2025).

The numerical code used to simulate dynamic rupture propagation is SEM2DPACK (Ampuero, 2012), an open-source research code available at https://github.com/jpampuero/sem2dpack.

Acknowledgments
F.P. and M.V. acknowledge support from the European Research Council Starting Grant project 757290-BEFINE. F.P. and F.P. acknowledge support from the European Research Council Starting Grant project HOPE 101041966. F.P. acknowledges support from the SNF PostDoc.Mobility Grant P500PN_222262. J.P.A. is supported by the French government through the UCAJEDI Investments in the Future project (ANR-15-IDEX-01) managed by the National Research Agency (ANR). The authors would like to thank Michel Teuscher and Laurent Morier from PLTE at EPFL for developing the large biaxial apparatus used in this study. The authors would like to thank reviewer Fabio Corbi for his insightful comments which greatly improved the manuscript, and an anonymous reviewer for their valuable suggestions.

References

Ampuero, J. P. (2012). Sem2dpack, a spectral element software for 2d seismic wave propagation and earthquake source dynamics [Software]. *Zenodo*, *v2.3.8*. https://doi.org/10.5281/zenodo.230363

Bakun, W., Aagaard, B., Dost, B., Ellsworth, W. L., Hardebeck, J. L., Harris, R. A., et al. (2005). Implications for prediction and hazard assessment from the 2004 parkfield earthquake. *Nature*, *437*(7061), 969–974. https://doi.org/10.1038/nature04067

Barbot, S. (2019). Slow-slip, slow earthquakes, period-two cycles, full and partial ruptures, and deterministic chaos in a single asperity fault. *Tectonophysics*, *768*, 228171. https://doi.org/10.1016/j.tecto.2019.228171

Bayart, E., Svetlizky, I., & Fineberg, J. (2016). Fracture mechanics determine the lengths of interface ruptures that mediate frictional motion. *Nature Physics*, *12*(2), 166–170. https://doi.org/10.1038/nphys3539

Bayart, E., Svetlizky, I., & Fineberg, J. (2018). Rupture dynamics of heterogeneous frictional interfaces. *Journal of Geophysical Research: Solid Earth*, *123*(5), 3828–3848. https://doi.org/10.1002/2018JB015509

Ben-David, O., & Fineberg, J. (2011). Static friction coefficient is not a material constant. *Physical Review Letters*, *106*(25), 1–4. https://doi.org/10.1103/PhysRevLett.106.254301

Brace, W. F., & Byerlee, J. D. (1966). Stick-slip as a mechanism for earthquakes. *Science*, *153*(3739), 990–992. https://doi.org/10.1126/science.153.3739.990

Buijze, L., Guo, Y., Niemeijer, A., Ma, S., & Spiers, C. (2020). Nucleation of stick-slip instability within a large-scale experimental fault: Effects of stress heterogeneities due to loading and gouge layer compaction. *Journal of Geophysical Research: Solid Earth*, *125*(8), e2019JB018429. https://doi.org/10.1029/2019jb018429

Buijze, L., Guo, Y., Niemeijer, A., Ma, S., & Spiers, C. (2021). Effects of heterogeneous gouge segments on the slip behavior of experimental faults at dm scale. *Earth and Planetary Science Letters*, *554*, 116652. https://doi.org/10.1016/j.epsl.2020.116652

Caniven, Y., Dominguez, S., Soliva, R., Peyret, M., Cattin, R., & Maerten, F. (2017). Relationships between along-fault heterogeneous normal stress and fault slip patterns during the seismic cycle: Insights from a strike-slip fault laboratory model. *Earth and Planetary Science Letters*, *480*, 147–157. https://doi.org/10.1016/j.epsl.2017.10.009

Cattania, C. (2019). Complex earthquake sequences on simple faults. *Geophysical Research Letters*, *46*(17–18), 10384–10393. https://doi.org/10.1029/2019GL083628

Cattania, C., & Segall, P. (2021). Precursory slow slip and foreshocks on rough faults. *Journal of Geophysical Research: Solid Earth*, *126*(4), e2020JB020430. https://doi.org/10.1029/2020JB020430

Cebry, S. B., Ke, C.-y., Shreedharan, S., Marone, C., Kammer, D. S., & Mclaskey, G. C. (2022). Creep fronts and complexity in laboratory earthquake sequences illuminate delayed earthquake triggering. *Nature Communications*, *13*, 1–9. https://doi.org/10.1038/s41467-022-34397-0

Cebry, S. B., Sorhaindo, K., & McLaskey, G. C. (2023). Laboratory earthquake rupture interactions with a high normal stress bump. *Journal of Geophysical Research: Solid Earth*, *128*(11), e2023JB027297. https://doi.org/10.1029/2023jb027297

Chen, X., Chitta, S. S., Zu, X., & Reches, Z. (2021). Dynamic fault weakening during earthquakes: Rupture or friction? *Earth and Planetary Science Letters*, *575*, 117165. https://doi.org/10.1016/j.epsl.2021.117165

Corbi, F., Mastella, G., Tinti, E., Rosenau, M., Sandri, L., Pardo, S., & Funiciello, F. (2024). Asperity size and neighboring segments can change the frictional response and fault slip behavior: Insights from laboratory experiments and numerical simulations. *Journal of Geophysical Research: Solid Earth*, *129*(1), e2023JB026594. https://doi.org/10.1029/2023JB026594

Dal Zilio, L., van Dinther, Y., Gerya, T., & Avouac, J. P. (2019). Bimodal seismicity in the himalaya controlled by fault friction and geometry. *Nature Communications*, *10*, 1–11. https://doi.org/10.1038/s41467-018-07874-8

Das, S., & Aki, K. (1977). Fault plane with barriers: A versatile earthquake model. *Journal of Geophysical Research*, *82*(36), 5658–5670. https://doi.org/10.1029/jb082i036p05658

Dieterich, J. H. (1978). Preseismic fault slip and earthquake prediction. *Journal of Geophysical Research*, *83*(8), 3940–3948. https://doi.org/10.1029/JB083iB08p03940

Dieterich, J. H. (1981). Potential for geophysical experiments in large scale tests. *Geophysical Research Letters*, *8*(7), 653–656. https://doi.org/10.1029/GL008i007p00653

Dublanchet, P., Bernard, P., & Favreau, P. (2013). Interactions and triggering in a 3-D rate-and-state asperity model. *Journal of Geophysical Research: Solid Earth*, *118*, 2225–2245. https://doi.org/10.1002/jgrb.50187

Freund, L. B. (1979). The mechanics of dynamic shear crack propagation. *Journal of Geophysical Research*, *84*(B5), 2199–2209. https://doi.org/10.1029/JB084iB05p02199

Fryer, B., Lebihain, M., Noël, C., Paglialunga, F., & Passelègue, F. (2024). The effect of stress barriers on unconventional-singularity-driven frictional rupture. *Journal of the Mechanics and Physics of Solids*, *193*, 105876. https://doi.org/10.1016/j.jmps.2024.105876

Gounon, A., Latour, S., Letort, J., & El Arem, S. (2022). Rupture nucleation on a periodically heterogeneous interface. *Geophysical Research Letters*, *49*(20), e2021GL096816. https://doi.org/10.1029/2021gl096816
Gualandi, A., Faranda, D., Marone, C., Cocco, M., & Mengaldo, G. (2023). Deterministic and stochastic chaos characterize laboratory earthquakes. *Earth and Planetary Science Letters*, *604*, 117995. https://doi.org/10.1016/j.epsl.2023.117995
Guérin-Marthe, S., Nielsen, S., Bird, R., Giani, S., & Di Toro, G. (2019). Earthquake nucleation size: Evidence of loading rate dependence in laboratory faults. *Journal of Geophysical Research: Solid Earth*, *124*(1), 689–708. https://doi.org/10.1029/2018JB016803
Gvirtzman, S., & Fineberg, J. (2021). Nucleation fronts ignite the interface rupture that initiates frictional motion. *Nature Physics*, *17*(9), 1037–1042. https://doi.org/10.1038/s41567-021-01299-9
Gvirtzman, S., & Fineberg, J. (2023). The initiation of frictional Motion—The nucleation dynamics of frictional ruptures. *Journal of Geophysical Research: Solid Earth*, *128*(2), e2022JB025483. https://doi.org/10.1029/2022jb025483
Iwashita, W., Matsukawa, H., & Otsuki, M. (2023). Static friction coefficient depends on the external pressure and block shape due to precursor slip. *Scientific Reports*, *13*(1), 2511. https://doi.org/10.1038/s41598-023-29764-w
Kammer, D. S., Radiguet, M., Ampuero, J. P., & Molinari, J. F. (2015). Linear elastic fracture mechanics predicts the propagation distance of frictional slip. *Tribology Letters*, *57*(3), 23. https://doi.org/10.1007/s11249-014-0451-8
Kaneko, Y., Avouac, J. P., & Lapusta, N. (2010). Towards inferring earthquake patterns from geodetic observations of interseismic coupling. *Nature Geoscience*, *3*(5), 363–369. https://doi.org/10.1038/ngeo843
Ke, C. Y., McLaskey, G. C., & Kammer, D. S. (2018). Rupture termination in laboratory-generated earthquakes. *Geophysical Research Letters*, *45*(23), 12784–12792. https://doi.org/10.1029/2018GL080492
Ke, C.-Y., McLaskey, G. C., & Kammer, D. S. (2020). The earthquake arrest zone. *Geophysical Journal International*, *224*(1), 581–589. https://doi.org/10.1093/gji/ggaa386
Lapusta, N., & Rice, J. R. (2003). Nucleation and early seismic propagation of small and large events in a crustal earthquake model. *Journal of Geophysical Research*, *108*(B4), 1–18. https://doi.org/10.1029/2001JB000793
Latour, S., Schubnel, A., Nielsen, S., Madariaga, R., & Vinciguerra, S. (2013). Characterization of nucleation during laboratory earthquakes. *Geophysical Research Letters*, *40*(19), 5064–5069. https://doi.org/10.1002/grl.50974
Lu, X., Lapusta, N., & Rosakis, A. J. (2007). Pulse-like and crack-like ruptures in experiments mimicking crustal earthquakes. *Proceedings of the National Academy of Sciences*, *104*(48), 18931–18936. https://doi.org/10.1073/pnas.0704268104
Mastella, G., Corbi, F., Bedford, J., Funiciello, F., & Rosenau, M. (2022). Forecasting surface velocity fields associated with laboratory seismic cycles using deep learning. *Geophysical Research Letters*, *49*(15), e2022GL099632. https://doi.org/10.1029/2022GL099632
Mclaskey, G. (2019). Earthquake initiation from laboratory observations and implications for foreshocks. *Journal of Geophysical Research: Solid Earth*, *124*(12), 882–904. https://doi.org/10.1029/2019JB018363
Mclaskey, G. C., & Kilgore, B. D. (2013). Foreshocks during the nucleation of stick-slip instability. *Journal of Geophysical Research: Solid Earth*, *118*(6), 2982–2997. https://doi.org/10.1002/jgrb.50232
Mei, C., Barbot, S., & Wu, W. (2021). Period-multiplying cycles at the transition between stick-slip and stable sliding and implications for the parkfield period-doubling tremors. *Geophysical Research Letters*, *48*(7), e2020GL091807. https://doi.org/10.1029/2020gl091807
Mele Veedu, D., Giorgetti, C., Scuderi, M., Barbot, S., Marone, C., & Collettini, C. (2020). Bifurcations at the stability transition of earthquake faulting. *Geophysical Research Letters*, *47*(19), e2020GL087985. https://doi.org/10.1029/2020gl087985
Okubo, P., & Dieterich, J. (1981). Fracture energy of stick-slip events in a large scale biaxial experiment. *Geophysical Research Letters*, *8*(8), 887–890. https://doi.org/10.1029/gl008i008p00887
Okubo, P., & Dieterich, J. (1984). Effects of physical fault properties on frictional instabilities produced on simulated faults. *Journal of Geophysical Research*, *89*(B7), 5817–5827. https://doi.org/10.1029/JB089iB07p05817
Paglialunga, F., Passelegue, F., Ampuero, J. P., Latour, S., & Violay, M. (2025). Data set for: "stress distribution and seismic cycle complexity on a long laboratory fault" [Dataset]. *Zenodo*. https://doi.org/10.5281/zenodo.15167862
Paglialunga, F., Passelegue, F., Latour, S., Gounon, A., & Violay, M. (2023). Influence of viscous lubricant on nucleation and propagation of frictional ruptures. *Journal Of Geophysical Research-Solid Earth*, *128*(4), e2022JB026090. https://doi.org/10.1029/2022JB026090
Passelègue, F. X., Schubnel, A., Nielsen, S., Bhat, H. S., & Madariaga, R. (2013). From sub-Rayleigh to supershear ruptures during stick-slip experiments on crustal rocks. *Science*, *340*(6137), 1208–1211. https://doi.org/10.1126/science.1235637
Perfettini, H., Avouac, J.-P., Tavera, H., Kositsky, A., Nocquet, J.-M., Bondoux, F., et al. (2010). Seismic and aseismic slip on the central Peru megathrust. *Nature*, *465*(7294), 78–81. https://doi.org/10.1038/nature09062
Radiguet, M., Kammer, D. S., Gillet, P., & Molinari, J. F. (2013). Survival of heterogeneous stress distributions created by precursory slip at frictional interfaces. *Physical Review Letters*, *111*(16), 1–5. https://doi.org/10.1103/PhysRevLett.111.164302
Radiguet, M., Kammer, D. S., & Molinari, J. F. (2015). The role of viscoelasticity on heterogeneous stress fields at frictional interfaces. *Mechanics of Materials*, *80*(PB), 276–287. https://doi.org/10.1016/j.mechmat.2014.03.009
Rosakis, A. J., Samudrala, O., & Coker, D. (1999). Cracks faster than the shear wave speed. *Science*, *284*(5418), 1337–1340. https://doi.org/10.1126/science.284.5418.1337
Rubin, A. M., & Ampuero, J. P. (2005). Earthquake nucleation on (aging) rate and state faults. *Journal of Geophysical Research*, *110*(2), 1–24. https://doi.org/10.1029/2005JB003686
Rubino, V., Lapusta, N., & Rosakis, A. (2022). Intermittent lab earthquakes in dynamically weakening fault gouge. *Nature*, *606*(7916), 922–929. https://doi.org/10.1038/s41586-022-04749-3
Rubino, V., Rosakis, A., & Lapusta, N. (2020). Spatiotemporal properties of sub-rayleigh and supershear ruptures inferred from full-field dynamic imaging of laboratory experiments. *Journal of Geophysical Research: Solid Earth*, *125*(2), e2019JB018922. https://doi.org/10.1029/2019jb018922
Rubinstein, S. M., Barel, I., Reches, Z., Braun, O. M., Urbakh, M., & Fineberg, J. (2011). Slip sequences in laboratory experiments resulting from inhomogeneous shear as analogs of earthquakes associated with a fault edge. *Pure and Applied Geophysics*, *168*(12), 2151–2166. https://doi.org/10.1007/s00024-010-0239-1
Rubinstein, S. M., Cohen, G., & Fineberg, J. (2004). Detachment fronts and the onset of dynamic friction. *Nature*, *430*, 1005–1009. https://doi.org/10.1038/nature02830
Salditch, L., Stein, S., Neely, J., Spencer, B. D., Brooks, E. M., Agnon, A., & Liu, M. (2020). Earthquake supercycles and long-term fault memory. *Tectonophysics*, *774*, 228289. https://doi.org/10.1016/j.tecto.2019.228289
Selvadurai, P. A. (2019). Laboratory insight into seismic estimates of energy partitioning during dynamic rupture: An observable scaling breakdown. *Journal of Geophysical Research: Solid Earth*, *124*(11), 11350–11379. https://doi.org/10.1029/2018JB017194
Shimazaki, K., & Nakata, T. (1980). Time-predictable recurrence model for large earthquakes. *Geophysical Research Letters*, *7*(4), 279–282. https://doi.org/10.1029/gl007i004p00279

Sladen, A. a., Tavera, H., Simons, M., Avouac, J.-P., Konca, A., Perfettini, H., et al. (2010). Source model of the 2007 M_w 8.0 pisco, Peru earthquake: Implications for seismogenic behavior of subduction megathrusts. *Journal of Geophysical Research*, *115*(B2), B02405. https://doi.org/10.1029/2009jb006429

Svetlizky, I., & Fineberg, J. (2014). Classical shear cracks drive the onset of dry frictional motion. *Nature*, *509*(7499), 205–208. https://doi.org/10.1038/nature13202

Svetlizky, I., Kammer, D., Bayart, E., Cohen, G., & Fineberg, J. (2017). Brittle fracture theory predicts the equation of motion of frictional rupture fronts. *Physical Review Letters*, *118*(12), 125501. https://doi.org/10.1103/PhysRevLett.118.125501

Tal, Y., Rubino, V., Rosakis, A. J., & Lapusta, N. (2022). Dynamics and near-field surface motions of transitioned supershear laboratory earthquakes in thrust faults. *Journal of Geophysical Research: Solid Earth*, *127*(3), e2021JB023733. https://doi.org/10.1029/2021jb023733

Tinti, E., Spudich, P., & Cocco, M. (2005). Earthquake fracture energy inferred from kinematic rupture models on extended faults. *Journal of Geophysical Research*, *110*(12), 1–25. https://doi.org/10.1029/2005JB003644

Wang, L., Xu, S., Zhuo, Y., Liu, P., & Ma, S. (2024). Unraveling the roles of fault asperities over earthquake cycles. *Earth and Planetary Science Letters*, *636*, 118711. https://doi.org/10.1016/j.epsl.2024.118711

Wyss, M., Schorlemmer, D., & Wiemer, S. (2000). Mapping asperities by minima of local recurrence time: San jacinto-elsinore fault zones. *Journal of Geophysical Research*, *105*(B4), 7829–7844. https://doi.org/10.1029/1999jb900347

Xia, K., Rosakis, A. J., & Kanamori, H. (2004). Laboratory earthquakes: The sub-Rayleigh-to-supershear rupture transition. *Science*, *303*(5665), 1859–1861. https://doi.org/10.1126/science.1094022

Xu, L., Ji, C., Meng, L., Ampuero, J.-P., Yunjun, Z., Mohanna, S., & Aoki, Y. (2024). Dual-initiation ruptures in the 2024 noto earthquake encircling a fault asperity at a swarm edge. *Science*, *385*(6711), 871–876. https://doi.org/10.1126/science.adp0493

Yamashita, F., Fukuyama, E., Xu, S., Kawakata, H., Mizoguchi, K., & Takizawa, S. (2021). Two end-member earthquake preparations illuminated by foreshock activity on a meter-scale laboratory fault. *Nature Communications*, *12*(1), 1–11. https://doi.org/10.1038/s41467-021-24625-4

Yamashita, F., Fukuyama, E., Xu, S., Mizoguchi, K., Kawakata, H., & Takizawa, S. (2018). Rupture preparation process controlled by surface roughness on meter-scale laboratory fault. *Tectonophysics*, *733*, 193–208. https://doi.org/10.1016/j.tecto.2018.01.034